

Gravitational Radiation from Standing Accretion Shock Instability in Core-Collapse Supernovae

Kei Kotake¹, Naofumi Ohnishi², and Shoichi Yamada^{3,4}

¹*Division of Theoretical Astronomy, National Astronomical Observatory Japan, 2-21-1, Osawa, Mitaka, Tokyo, 181-8588, Japan*

`kkotake@th.nao.ac.jp`

²*Department of Aerospace Engineering, Tohoku University, 6-6-01 Aramaki-Aza-Aoba, Aoba-ku, Sendai, 980-8579, Japan*

³*Science & Engineering, Waseda University, 3-4-1 Okubo, Shinjuku, Tokyo, 169-8555, Japan*

⁴*Advanced Research Institute for Science and Engineering, Waseda University, 3-4-1 Okubo, Shinjuku, Tokyo, 169-8555, Japan*

ABSTRACT

We present the results of numerical experiments, in which we study how the asphericities induced by the growth of the standing accretion shock instability (SASI) produce the gravitational waveforms in the postbounce phase of core-collapse supernovae. To obtain the neutrino-driven explosions, we parameterize the neutrino fluxes emitted from the central protoneutron star and approximate the neutrino transfer by a light-bulb scheme. We find that the waveforms due to the anisotropic neutrino emissions show the monotonic increase with time, whose amplitudes are up to two order-of-magnitudes larger than the ones from the convective matter motions outside the protoneutron stars. We point out that the amplitudes begin to become larger when the growth of the SASI enters the non-linear phase, in which the deformation of the shocks and the neutrino anisotropy become large. From the spectrum analysis of the waveforms, we find that the amplitudes from the neutrinos are dominant over the ones from the matter motions at the frequency below ~ 100 Hz, which are suggested to be within the detection limits of the detectors in the next generation such as LCGT and the advanced LIGO for a supernova at 10 kpc. As a contribution to the gravitational wave background, we show that the amplitudes from this source could be larger at the frequency above ~ 1 Hz than the primordial gravitational wave backgrounds, but unfortunately, invisible to the proposed space-based detectors.

Subject headings: supernovae: collapse — neutrinos — hydrodynamics — instability

1. Introduction

The gravitational astronomy is now becoming a reality. In fact, the ground-based laser interferometers such as TAMA300 (Ando & the TAMA collaboration 2002; Ando et al. 2005) and the first LIGO (Thorne 1995; Abbott et al. 2005) are beginning to take data at sensitivities where astrophysical events are predicted. For the detectors including GEO600 and VIRGO, core-collapse supernovae especially in our Galaxy, have been supposed to be the most plausible sources of gravitational waves (see, for example, New (2003); Kotake et al. (2006) for review). Since the gravitational wave (plus neutrinos) is the only tool which gives us the information in the innermost part of evolved massive stars, the detection is important not only for the direct confirmation of gravitational waves but also for the understanding of supernova physics itself.

So far, most of the theoretical predictions of gravitational waves from supernovae have focused on the bounce signal in the context of rotational (Mönchmeyer et al. 1991; Yamada & Sato 1995; Zwerger & Mueller 1997; Dimmelmeier et al. 2002; Fryer et al. 2002; Kotake et al. 2003; Shibata & Sekiguchi 2004; Ott et al. 2004) and magnetorotational (Kotake et al. 2004; Obergaulinger et al. 2006) core collapse. In most of the previous studies, the iron core prior to core-collapse was assumed to rotate much more rapidly than predicted by the recent stellar evolution calculations (Heger et al. 2005). Recently, the initial rotation periods were estimated to be larger than ~ 100 sec for the observed rotation periods of the radio pulsars (Ott et al. 2006). In such a slowly rotating case, the bounce signal becomes too small to be detected even by the laser interferometers in the next generation for a galactic supernova, owing to the suppression of the rotation-induced deformation at core-bounce (see, e.g., Kotake et al. (2004)).

Besides the rapid rotation of the cores, two other ingredients have been considered to be important in the much later phases after core bounce, namely convective motions and anisotropic neutrino emissions. Both of them contribute to the non-spherical parts in the energy momentum tensor of the Einstein equations, thus being the potential sources of the gravitational wave (see, Kotake et al. (2006) for a review). One of the possibility as the origin of the asphericities may be large scale density inhomogeneities formed in the central core prior to collapse (e.g., Bazan & Arnett (1998); Meakin & Arnett (2006)). Fryer (2004) performed three dimensional SPH simulations and pointed out that the neutrino-originated gravitational waves, which dominate over the one from the convections, are within

the detection limits for the advanced LIGO for the galactic supernova (see also, Burrows & Hayes (1996); Fryer (2004); Fryer et al. (2004); Müller & Janka (1997)). Another possibility to induce anisotropy is the (moderate) rotation of the core. Müller et al. (2004) calculated the gravitational waves based on the two-dimensional (2D) Boltzmann transport simulations of slowly rotating core (Buras et al. 2003) and found that the neutrino-originated gravitational waves exceed the bounce signal large enough to be detectable by the advanced LIGO with good signal-to-noise ratio for the galactic supernova (see, also Kotake et al. (2006) for the properties of neutrino-originated gravitational waves in the rapidly rotating case). More recently, the new ingredient of the gravitational-wave emissions is reported (Ott et al. 2006), namely the g-mode excitations of the protoneutron stars, which was observed in the 2D approximate Boltzmann transport simulations at much later postbounce phase (~ 600 ms) (Burrows et al. 2006).

There is another ingredient for producing large asphericity, to which much attention has been paid recently in the context of the studies about the explosion mechanisms, that is the so-called standing accretion shock instability (often called “SASI”). In the numerical simulations by Blondin et al. (2003); Scheck et al. (2004); Blondin & Mezzacappa (2006); Ohnishi et al. (2006a,b), it was found that the standing shock wave is shown to be unstable to non-radial perturbations, and that the perturbations grow up to the non linear regime with clear low-mode ($\ell = 1, 2$) dominance, leading to the global deformation of the shock wave later. Here ℓ stands for the azimuthal index of the Legendre polynomials. The importance of SASI is also stressed by the recent studies, demonstrating that such an explosion is favorable to reproduce the observed synthesized elements of SN1987A (Kifonidis et al. 2006) and also to explain the origin of the natal kicks of young pulsars (Scheck et al. 2004). These situations motivate us to study how the gravitational waveforms are originated from the asphericities by SASI.

In this paper, we present the results of numerical experiments, in which we study how the asphericities induced by the growth of SASI produce the gravitational waveforms. To obtain the neutrino-driven explosions, we parameterize the neutrino fluxes emitted from the central protoneutron star and approximate the neutrino transfer by the light-bulb scheme. Based on the long-term two dimensional hydrodynamic results, we calculate the gravitational waveforms. By doing the spectrum analysis, we study the detectability of such signals from a nearby core-collapse supernova. It is noted that much attention has been paid recently to the core-collapse supernovae as one of the promising sources of the cosmological gravitational wave backgrounds (see, e.g., Buonanno et al. (2005) and references therein). Thus we calculate the SASI-induced gravitational wave backgrounds and discuss the detectability by

the currently proposed space-based detectors such as LISA¹, BBO², and DECIGO (Seto et al. 2001).

The plan of this paper is as follows: In Section 2, we outline the initial models, the numerical methods, and shortly summarize the methods for calculating the waveforms. We show the main numerical results in Section 3. We summarize and discuss our results in Section 4.

2. Numerical Methods and Models

2.1. Initial Models and Hydrodynamics

The numerical methods employed in this paper are essentially the same as those used in our previous paper (Ohnishi et al. 2006a). The basic evolution equations, describing the compressible accretion flows of matter attracted by the protoneutron star and irradiated by neutrinos emitted from the neutrino sphere, are written as follows,

$$\frac{d\rho}{dt} + \rho \nabla \cdot \mathbf{v} = 0, \quad (1)$$

$$\rho \frac{d\mathbf{v}}{dt} = -\nabla P - \rho \nabla \Phi, \quad (2)$$

$$\rho \frac{d}{dt} \left(\frac{e}{\rho} \right) = -P \nabla \cdot \mathbf{v} + Q_E + Q_{\text{inel}} - Q_{\nu\bar{\nu}} - Q_{\text{brems}} - Q_{\text{plasmon}}, \quad (3)$$

$$\frac{dY_e}{dt} = Q_N, \quad (4)$$

$$\Phi = -\frac{GM_{\text{in}}}{r}, \quad (5)$$

where $\rho, \mathbf{v}, e, P, Y_e, \Phi$ are density, velocity, internal energy, pressure, electron fraction, and gravitational potential, respectively. We denote the Lagrangian derivative as d/dt and r is the radius. M_{in} is the mass of the central object. The self-gravity of matter in the accretion flow is ignored (see Yamasaki & Yamada (2006) for the effect). The parameters of Q_E and Q_N are related to the standard heating and cooling via neutrino absorptions and emissions by free nucleons (see also Ohnishi et al. (2006a)). Q_{inel} is the minor additional heating by the inelastic neutrino-helium interactions estimated by Haxton (1988) as considered in Ohnishi

¹see <http://lisa.jpl.nasa.gov/>

²see <http://universe.nasa.gov/program/bbo.html>

et al. (2006b). In addition, we newly take into account the neutrino cooling by neutrino pair annihilation to e^-e^+ pairs ($: Q_{\nu\bar{\nu}}$), nucleons-nucleons bremsstrahlung ($: Q_{\text{brems}}$) (Hannestad & Raffelt 1998; Burrows et al. 2000), and plasmon decay into $\nu_e, \bar{\nu}_e$ ($: Q_{\text{plasmon}}$) (Schinder et al. 1987; Ruffert et al. 1996).

The numerical code employed in this paper is based on the modified version of the ZEUS-2D (Stone & Norman 1992) for the applications to the supernova studies (Kotake et al. 2003), in which the tabulated realistic equation of state (EOS) based on the relativistic mean field theory (Shen et al. 1998) was implemented. Furthermore, we have added the equation for electron fraction (Eq. (4)) and included the neutrino coolings/heatings parametrically as the source term of the energy equations (Eq. (3)), both of which are solved in the operator-splitting fashion. In the simulations, spherical coordinates are used without imposing the equatorial symmetry. The computation domain covers the whole meridian section with 60 angular mesh points, except for a model in which we have adopted 120 angular grid points. Since the latter model did not produce any significant difference from other models, we will report in the following the results obtained from the models with 60 angular mesh points. We use 300 radial mesh points to cover $r_{\text{in}} \leq r \leq r_{\text{out}} = 2000$ km, where r_{in} is the inner boundary and chosen to be roughly the radius of neutrino sphere.

The initial conditions are provided in the same manner of Ohnishi et al. (2006a) as the steady state solution of Yamasaki & Yamada (2005). In constructing the initial conditions, we assume a fixed density $\rho_{\text{in}} = 10^{11}$ g cm $^{-3}$ at the inner boundary. And the initial mass accretion rates and the initial mass of the central object are set to be $\dot{M} = 1 M_{\odot} \text{ s}^{-1}$ and $M_{\text{in}} = 1.4 M_{\odot}$, respectively. To induce the non-spherical instability, we have added $\ell = 1$ velocity perturbations to the initial state mentioned above. At the outer boundary, we adopt the fixed boundary condition consistent with the initial condition. On the other hand, the absorbing boundary is used at the inner boundary. The temperatures of electron-type neutrinos are also constant and set to be $T_{\nu_e} = 4$ MeV and $T_{\bar{\nu}_e} = 5$ MeV, which are the typical values in the post-bounce phase. The temperature of mu and tau neutrinos is chosen to be $T_{\nu_{\mu}} = 10$ MeV. In the standard model, the luminosity of electron-type neutrino L_{ν_e} and anti-neutrino $L_{\bar{\nu}_e}$ are set to be 6.5×10^{52} ergs s $^{-1}$. In addition, we examined two cases of lower luminosities of $L_{\nu_e} = L_{\bar{\nu}_e} = 6.0, 5.5 \times 10^{52}$ ergs s $^{-1}$. In all the computed models, the luminosity of mu and tau neutrinos is set to be half value of electron-type neutrinos, keeping consistency with the results obtained by the previous detailed numerical studies (e.g., Liebendörfer et al. (2001)).

2.2. Computations of gravitational wave signals

We follow the methods based on Epstein (1978); Müller & Janka (1997); Burrows & Hayes (1996); Kotake et al. (2006) in order to compute the gravitational waveform from anisotropic neutrino emissions. We will summarize it in the following for convenience. Since we assume axisymmetry, the transverse-traceless gravitational field h^{TT} is shown to have one nonvanishing component for the observer in the equatorial plane:

$$h_{\nu}^{\text{TT}} = \frac{4G}{c^4 R} \int_0^t dt' \int_0^{\pi} d\theta' \Phi(\theta') \frac{dl_{\nu}(\theta', t')}{d\Omega'}, \quad (6)$$

where G is the gravitational constant, c is the speed of light, R is the distance of the source to the observer, $dl_{\nu}/d\Omega$ represents the direction-dependent neutrino luminosity emitted per unit of solid angle into direction of Ω , and $\Phi(\theta')$ denotes the quantity, which depends on the angle measured from the symmetry axis (θ') (see Figure 1),

$$\Phi(\theta') = \sin \theta' \left(-\pi + \int_0^{2\pi} d\phi' \frac{1 + \sin \theta' \cos \phi'}{1 + \tan^2 \theta' \sin^2 \phi'} \right) \quad (7)$$

$$= \pi \sin \theta' (-1 + 2|\cos \theta'|). \quad (8)$$

The integration with respect to the azimuthal angle (ϕ'), albeit fairly straightforward, is pretty helpful to the later discussions, which is not published to our knowledge. In addition, from Eq. (8), one can readily see that no gravitational waves are emitted if the neutrino radiation is isotropic. We estimate $dl_{\nu}/d\Omega$ as follows,

$$\frac{dl_{\nu}}{d\Omega}(\theta') = \int_0^{r_{\text{out}}} dr r^2 |Q_{\text{C}}|_{\text{calculated at each } \theta'}, \quad (9)$$

where Q_{C} is the sum of contributions from the neutrino coolings, of each species (ν_e , $\bar{\nu}_e$, $\nu_{\mu,\tau}$, and $\bar{\nu}_{\mu,\tau}$) computed from the source term of Eq. (3). In the above estimation, neutrinos are assumed to be emitted radially in each angular bin. As a guide to see the anisotropy of the neutrino emissions, we calculate the anisotropy parameter according to Müller & Janka (1997) as follows,

$$\alpha(t) = \frac{1}{l_{\nu}(t)} \int_0^{\pi} d\theta' \Phi(\theta') \frac{dl_{\nu}(\theta', t)}{d\Omega'}. \quad (10)$$

It should be noted that the gravitational waves from neutrinos have a different feature from the ones from matter motions, in the sense that the former has *memory effect*, which means that the gravitational amplitude jumps from zero to a nonvanishing value and it keeps the non-vanishing value even after the energy source of gravitational waves disappeared (see Braginskii & Thorne (1987) for details, and Segalis & Ori (2001); Hiramatsu et al. (2005)

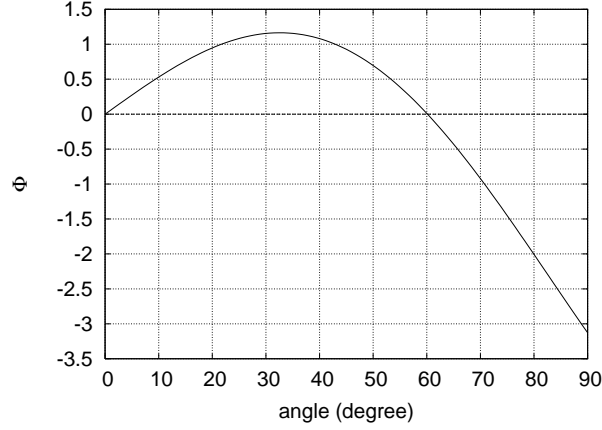


Fig. 1.— Angular dependence of Φ in Eq. (8). Note that the angle is measured from the symmetry axis.

for the examples of the astrophysical emitters of such gravitational waves and references therein). In Eq. (6), this nature can be directly seen as the time-integral.

As for the gravitational waves, $h(t)$, of the quadrupole radiation of mass motions, we employ the standard strain formula,

$$h(t) = \frac{1}{8} \left(\frac{15}{\pi} \right)^{1/2} \sin^2 \alpha \frac{A_{20}^{E2}}{R}, \quad (11)$$

where the form of A_{20}^{E2} can be found in references (see equation (12) in Mönchmeyer et al. (1991)). In using the formula, the azimuthal gradient of the gravitational potential is set to be zero, since we neglect the self-gravity of the computational domain and treat the gravity as in Eq. (5). In the following computations, we assume that the observer is located in the equatorial plane since the most of gravitational wave is radiated in the plane ($\alpha = \pi/2$ in Eq. (11)), and that the source is assumed to be located at our galactic center ($R = 10$ kpc). In order to assess the detectability of the gravitational waves obtained in this study, we employ the characteristic gravitational wave strain,

$$h_c(f) = \frac{1}{R} \sqrt{\frac{2}{\pi^2} \frac{G}{c^3} \frac{dE_{\text{GW}}(f)}{df}}, \quad (12)$$

for a given frequency f (Flanagan & Hughes 1998). Here $dE_{\text{GW}}(f)/df$ is the energy spectra of gravitational waves defined as follows,

$$\frac{dE_{\text{GW}}(f)}{df} = \frac{c^3}{G} \frac{(2\pi f)^2}{16\pi} \left| \tilde{A}_{20}^{E2}(f) \right|^2 \quad (13)$$

We employ the Fast Fourier Transformation technique in order to perform the Fourier transformation of $A_{20}^{E2}(t)$ to $\tilde{A}_{20}^{E2}(f)$.

We discuss the contribution of the gravitational waves mentioned above to the cosmological background gravitational radiation. For simplicity, we assume that all core-collapse supernovae have identical emission characteristics. According to Phinney (2001); Buonanno et al. (2005), the density parameter, which represents the sum of energy densities radiated by a large number of independent core-collapse supernovae at each redshift, can be written as,

$$\Omega_{\text{gw}}(f) = \frac{1}{\rho_c c^2} \int_0^\infty dz \frac{R_{\text{SN}}(z)}{1+z} \left| \frac{dt}{dz} \right| f_z \frac{dE_{\text{GW}}}{df}(f_z), \quad (14)$$

where $\rho_c = 3H_0^2/(8\pi G)$ is the cosmic critical density, $R_{\text{SN}}(z)$ is the event rate of core-collapse supernovae per comoving volume, and $f_z \equiv (1+z)f$. The cosmological model enters with $|dt/dz| = [(1+z)H(z)]^{-1}$ and, for a flat geometry,

$$H(z) = H_0 [\Omega_M(1+z)^3 + \Omega_\Lambda]^{1/2}. \quad (15)$$

We will use the parameters $\Omega_M = 0.3$, $\Omega_\Lambda = 0.7$, and $H_0 = h_0 100 \text{ km s}^{-1} \text{ Mpc}^{-1}$ with $h_0 = 0.72$. As for the core-collapse supernova rate, we employ the parameterization by Buonanno et al. (2005) as follows,

$$R_{\text{SN}}(z) = R_{\text{SN}}^0 \times \begin{cases} (1+z)^\beta & \text{for } z < 1 \\ 2^{\beta-\alpha}(1+z)^\alpha & \text{for } 1 \leq z \leq 20 \end{cases}. \quad (16)$$

We take $\beta = 2.7$ and the present-day rate $R_{\text{SN}}^0 = 2 \times 10^{-4} \text{ Mpc}^{-3} \text{ yr}^{-1}$, which are consistent with the Super-K limits on the diffuse neutrino background (Malek et al. 2003). Since the parameter $0 \lesssim \alpha \lesssim 2$ is much less constrained than β and R_{SN}^0 (see, for example, Ando & Sato (2004) and references therein), we examine the two cases of $\alpha = 0, 2$ in the later discussion.

3. Results

Only in the case of $L_{\nu_e} = 6.5 \times 10^{52} \text{ erg s}^{-1}$, we can observe the continuous increase of the average shock radius, reaching the outer boundary of the computational domain (2000 km in radius) in ~ 500 ms with the explosion energy of 4.0×10^{50} ergs. In other models, we terminate the simulations at about 1 sec, not seeing the increase of the shock radius. Bearing in mind the evidences that the SASI-induced explosions are favorable for explaining the observed quantities of supernovae mentioned earlier, we take the exploding model of $L_\nu = 6.5 \times 10^{52} \text{ erg s}^{-1}$ as a reference in the following. For later convenience, the values of several important quantities are summarized in Table 1.

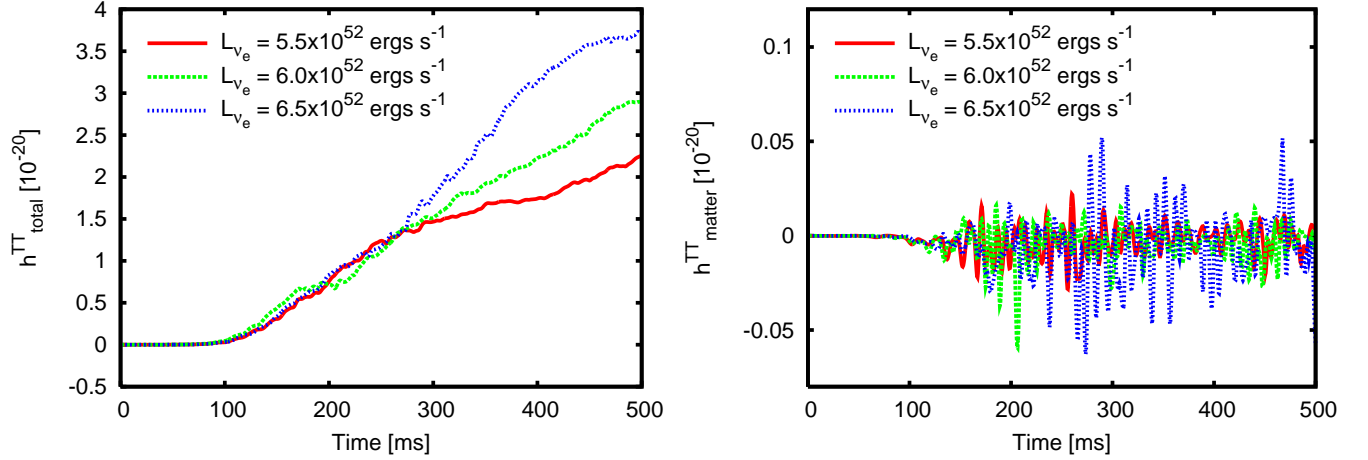


Fig. 2.— Gravitational waveforms from the sum of the anisotropic neutrino emissions and the matter motions (left panel) and only from the matter motions (right panel). The time is measured from the epoch when the neutrino luminosity is injected from the surface of the neutrino sphere. Note that the supernova is assumed to be located at the distance of 10 kpc.

3.1. Properties of Waveform

In the left panel of Figure 2, the total amplitudes including the contributions both from the anisotropic neutrino emissions and the matter motions, are shown. Comparing the right panel, in which the amplitudes only from the matter motions are shown, we can see the neutrino-originated gravitational waves are up to two order-of-magnitudes larger than those from the matter motions during the SASI operation (at $t \gtrsim 200$ ms as explained shortly). This reflects the small mass in the regions outside the neutrino sphere in the postbounce

Table 1. Model Summary

L_ν (10^{52} erg/s)	Δt (ms)	E_{GW} ($M_\odot c^2$)	f_{eq} (Hz)	h_{eq}
6.5	540	6.1×10^{-10}	51.0	5.3×10^{-22}
6.0	1000	4.6×10^{-10}	59.0	7.0×10^{-22}
5.5	1000	2.3×10^{-10}	63.2	5.1×10^{-22}

Note. — L_ν denotes the input luminosity. Δt represents the simulation time. E_{GW} is the total radiated energy in the form of gravitational waves in unit of $M_\odot c^2$. f_{eq} and h_{eq} represents the frequency, and amplitude, under which the gravitational waves from anisotropic neutrino emissions dominate the ones from the matter motions, respectively. Note that the supernova is assumed to be located at the distance of 10 kpc.

phase (at most $0.1M_{\odot}$ throughout the simulation time). In the following, we pay attention to the neutrino-originated gravitational wave.

Looking at the left panel of Figure 2, the waveforms show the monotonic increase with time regardless of the input neutrino luminosities. To understand this trend, we look into the hydrodynamical behaviors induced by the SASI, taking the case of $L_{\nu_e} = 6.5 \times 10^{52}$ erg s $^{-1}$.

In Figure 4, snapshots showing the hydrodynamical features with the resulting gravitational wave amplitudes (inserted figures) are shown. Up to ~ 100 ms after the onset of the simulation, no significant changes in the amplitudes and no deviations of the dynamics from spherical symmetry are found. It is noted that no gravitational waves are emitted when the motion of the regions outside is spherical, since the neutrino luminosity from the center is taken to be isotropic.

After ~ 100 ms, the regions outside the neutrino sphere begin to oscillate with increasing average radius and wave amplitudes. The reason why the sign of the growing amplitudes is positive is as follows. From the angular dependence of Φ in Figure 1 and Eq. (8), it can be seen that the neutrino emissions from the regions with θ' smaller than $\pi/3$ contribute to the positive amplitude, while the negative sign comes from the regions from $\pi/3$ to $\pi/2$. It is noted that this feature is north-south symmetric (Eq. (8)). Due to the dominance of $l = 1, 2$ modes of the deformed shock waves during the SASI operation mentioned below, the neutrino emissions become stronger in the regions close to the symmetry axis. By these two factors, the amplitudes are found to increase monotonically with time. This property is common to the lower luminosity models as seen from the left panel of Figure 2. As a side-remark, the contribution of each neutrino species to the waveform is presented in Figure 3, which also shows the dominant contribution from ν_e .

Next we discuss in more detail how the features of the waveforms are related to the growth of the SASI. For the purpose, we decompose the fluctuations of the shock surface into the spherical harmonic components;

$$R_s(\theta) = \sum_{\ell=0}^{\infty} a_{\ell} \sqrt{\frac{2\ell+1}{4\pi}} P_{\ell}(\cos \theta). \quad (17)$$

Since the system is axisymmetric, only $m = 0$ harmonics, that is Legendre polynomials, show up. The coefficients, a_{ℓ} , can be calculated by the orthogonality of the Legendre polynomials;

$$a_{\ell} = \frac{2\ell+1}{2} \int_{-1}^1 R_s(\theta) P_{\ell}(\cos \theta) d \cos \theta. \quad (18)$$

The position of the shock surface, $R_s(\theta)$, is estimated from the iso-entropic surface of $s = 5$. The left panel of Figure 5 shows the evolution of the amplitude of each mode ($\ell = 1, 2$)

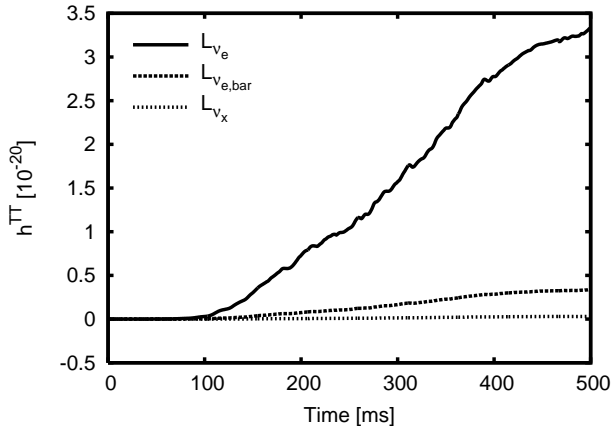


Fig. 3.— Contribution of each neutrino species to the waveform for the case of $L_{\nu_e} = 6.5 \times 10^{52} \text{ erg s}^{-1}$. Here ν_X represents μ, τ neutrinos. It is noted that the qualitative features are common to the other cases.

normalized by the average shock radius of a_0 . The dominance of the fundamental mode ($\ell = 1$) initially is simply due to the initial velocity perturbation assumed in this simulation. From ~ 40 ms, $\ell = 2$ begins to develop rapidly and at ~ 200 ms, the amplitude becomes of the same order as that of the fundamental mode, which has already been saturated by this time. This marks the beginning of the nonlinear phase.

This transition from linear to nonlinear phase corresponds to the time of the rapid increase of the average shock radius as seen from the top right (~ 200 ms) to middle left panel (~ 270 ms) in Figure 4. Simultaneously, this makes the deformation of the shock more elongated along the symmetry axis, leading to the slightly steep rise of the neutrino-originated gravitational wave afterwards for the reason mentioned above (see the left panel of Figure 2). Here it should be noted that the dominance of $\ell = 2$ mode induces the rapid increase of the gravitational waves from the matter motions, albeit its amplitudes being very small, and is clearly understood from the quadrupole nature of gravitational radiations (compare the left and right panels of Figure 5).

The anisotropy parameter $\alpha(t)$ in Eq.(10) also helps us to see the relation between the anisotropy of the neutrino radiation fields and the properties of the waveforms. The time evolution of α is presented in Figure 6. In case of $L_{\nu_e} = 6.5 \times 10^{52} \text{ erg s}^{-1}$, α takes larger values after the saturation, leading to more greater wave amplitudes. In the right panel of Figure 6, the ratios of the wave amplitudes of $L_{\nu_e} = 6.5 \times 10^{52} \text{ erg s}^{-1}$ and $L_{\nu_e} = 6.0 \times 10^{52} \text{ erg s}^{-1}$ to $L_{\nu_e} = 5.5 \times 10^{52} \text{ erg s}^{-1}$, are shown. Only near after the nonlinear phase sets in (~ 200 ms), it is seen that the SASI-induced anisotropy of the neutrino emissions determines the waveforms, whose amplitudes monotonically grow with time. As a reference, we draw the

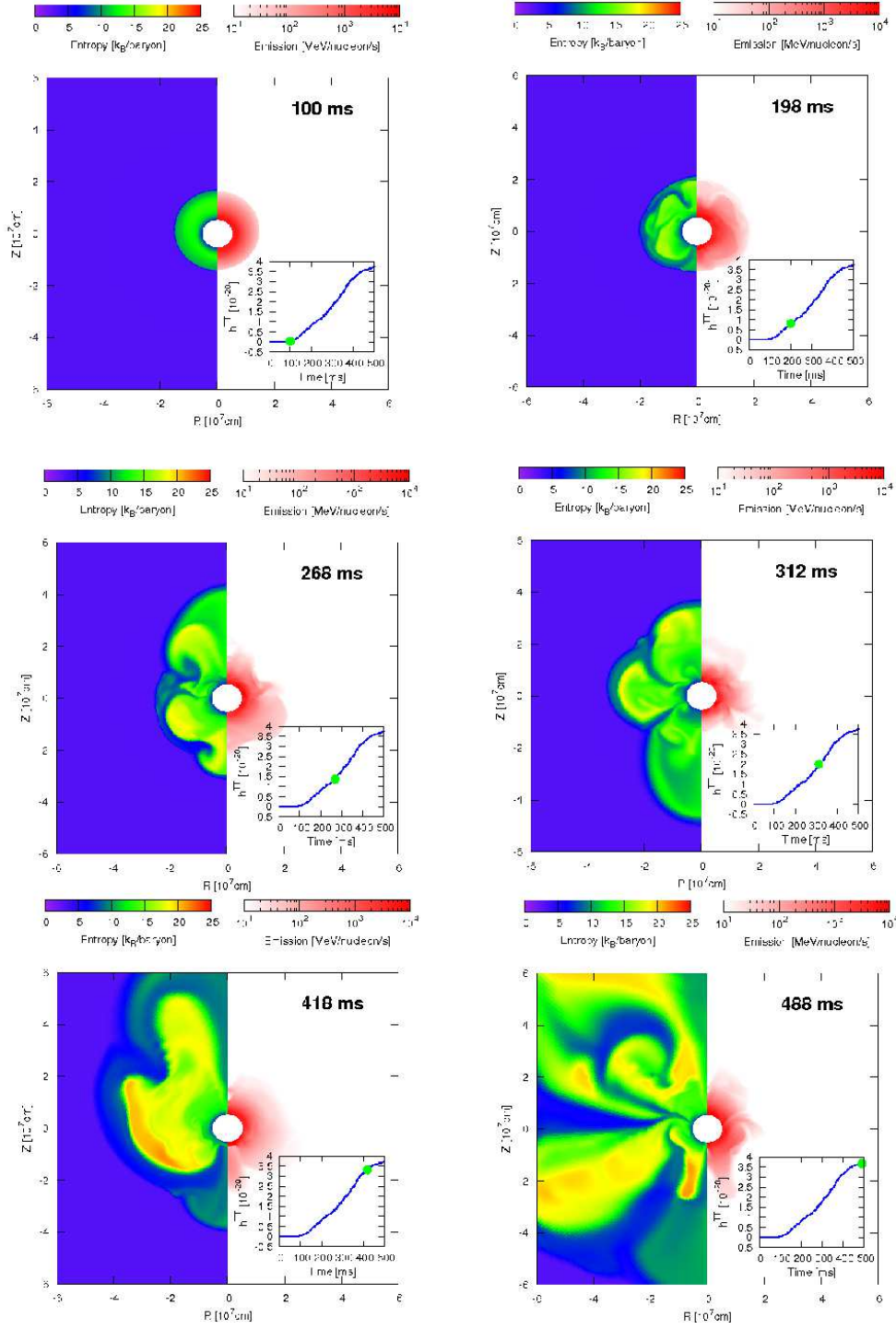


Fig. 4.— Entropy- (the left half panel of each panel) and net neutrino emissivity- (the right half) distributions in the meridian section for the case of $L_{\nu_e} = 6.5 \times 10^{52} \text{ erg s}^{-1}$. The insert of each panel shows the wave amplitudes, in which the green point indicates the time of the snapshot.

lines indicating the ratio of the input neutrino luminosities. It can be also seen that the increase of the amplitudes is greater than the one estimated only by the difference of the input luminosities after the onset of the nonlinear phase.

Finally, we have to discuss whether the above discussions are subject to change when the numerical resolution becomes more better. In Figure 7, we compare the waveforms when the angular resolution is doubled in comparison with the model computed so far. As easily guessed, the difference appears after the SASI saturates (~ 200 ms) and the non-linear phase sets in. In the lower resolution calculation, the anisotropy of the shock propagation tends to become more larger than the high resolution case, which results in the larger neutrino anisotropy, and thus leading to the larger wave amplitudes. The difference is not greater than $\sim 20\%$, and thus the qualitative features discussed so far are found to be unchanged.

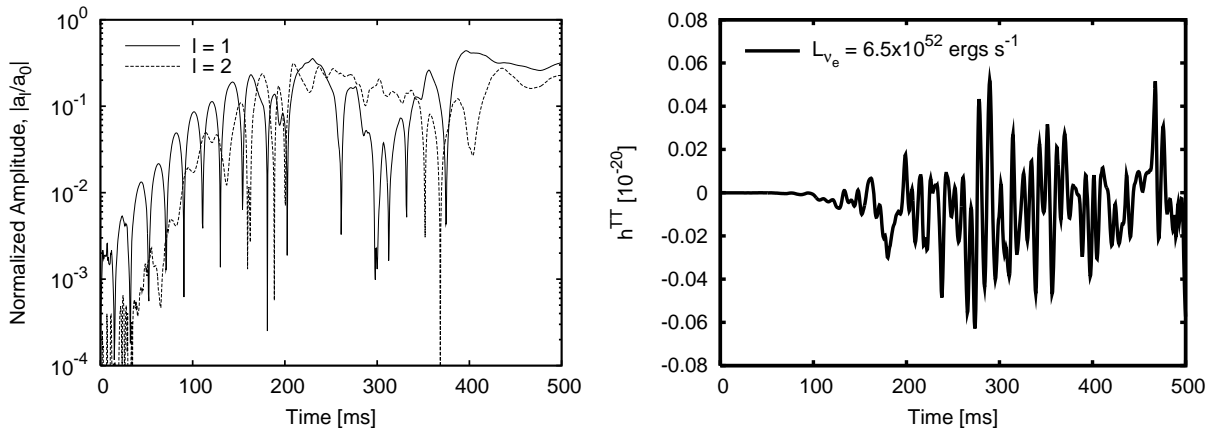


Fig. 5.— Time evolution of the normalized amplitudes of $\ell = 1, 2$ modes (left) and the waveform from the matter motions (right) for the case of $L_{\nu_e} = 6.5 \times 10^{52}$ erg s $^{-1}$.

3.2. Spectrum Analysis

Now we move on to discuss the features of the waveforms by the spectrum analysis. From Figure 8, one can see the dominance of the neutrino-originated gravitational waves at lower frequency of ~ 100 Hz. As seen in the left panel of Figure 2, the waveform from the neutrino shows a long-time variability in comparison with the rapidly varying ($O(\text{ms})$) waveforms from matter motions, which is due to the local hydrodynamical instabilities. It is the memory effect of the neutrino-originated gravitational waves mentioned earlier that absorbs the rapid time variations of the neutrino anisotropy.

To see clearly the dominance of the neutrino-originated gravitational wave than the

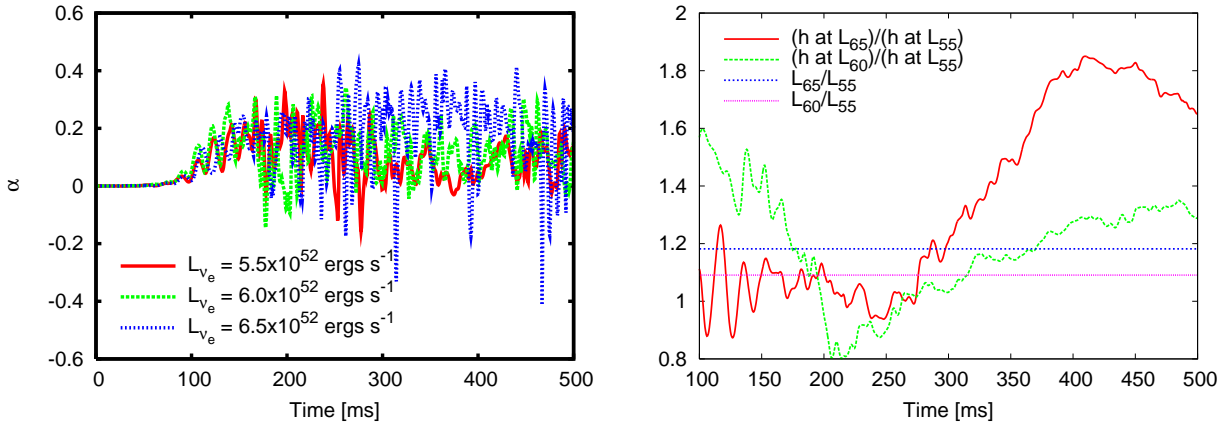


Fig. 6.— Time evolution of the neutrino anisotropy parameter (see Eq. (10)) (left) and the ratios of the wave amplitudes normalized by the case of the lowest input luminosity of $L_{\nu_e} = 5.5 \times 10^{52} \text{ erg s}^{-1}$ (denoted as L_{55}) (right). The horizontal lines in the right panel just represent the constant ratio of the input luminosity.

matter-originated one at the lower frequency, we define f_{eq} , the frequency below which the dominance occurs, and the corresponding gravitational wave amplitude, h_{eq} (see Table 1). From the table, it is found that the typical frequency is smaller for the higher luminosity case. In Figure 9, the gravitational wave spectra are plotted with the sensitivity curves of the laser interferometers. It can be seen that the detection of the gravitational wave at the low frequency range becomes more promising thanks to the contributions from the neutrinos. It can be seen that the gravitational waves from the neutrinos, which are dominated below $\sim 100 \text{ Hz}$, seem marginally within the detection limits of the currently running detector of the first LIGO and the detection seems more feasible for the detectors in the next generation such as LCGT and the advanced LIGO if a supernova occurs in our galactic center.

Finally, we are in a position to discuss the contribution of the gravitational waves mentioned so far to the background gravitational radiation. We calculate Ω_{gw} from Eqs. (13) and (14) for the highest luminosity case of $L_{\nu} = 6.5 \times 10^{52} \text{ erg s}^{-1}$. The resulting amplitude is presented in Figure 10. For the frequency greater than $\sim 100 \text{ Hz}$, the signal is dominated by the contribution from matter motions, while at lower frequencies the signal is dominated by the one from the neutrinos (compare Figure 9). “Low rate” and “High rate” in the figure correspond to the cases of $\alpha = 0, 2$ in Eq. (16), respectively, indicating the uncertainty of the core-collapse supernova rate as mentioned before. We terminated the simulation for the high luminosity case (see Table 1), seeing the shock wave propagate out of the iron core. For the frequencies of $f \ll (2\pi\Delta t)^{-1} \sim 0.1 \text{ Hz}(\Delta t/500 \text{ ms})^{-1}$ obtained from our simulations, we extended the spectra using the zero frequency limit (Turner 1978)

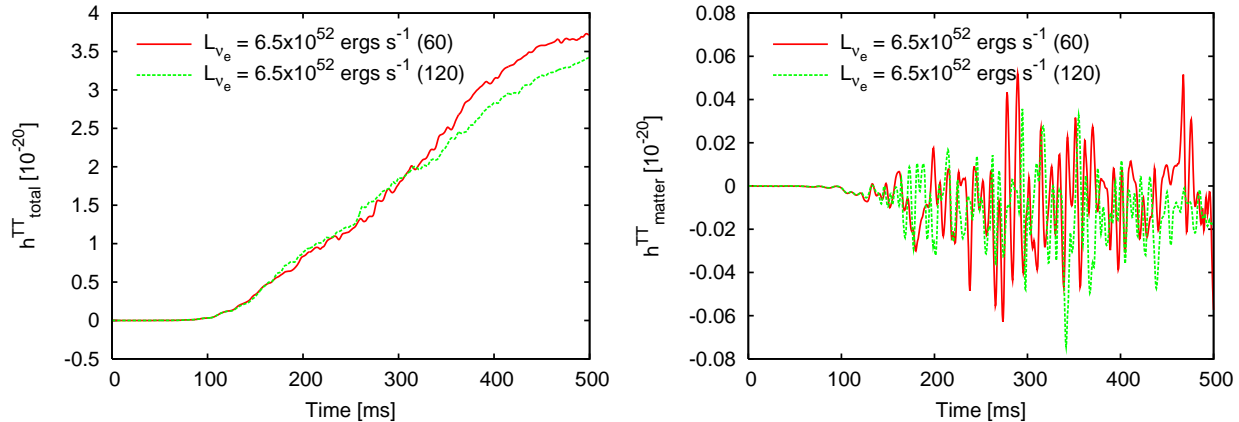


Fig. 7.— Effects of numerical resolutions on the waveforms. 60, 120 in the panel represents the number of the angular mesh points in the computational domain. Left and right panel shows the waveforms from the sum of the anisotropic neutrino emissions and only from the matter motions, respectively. After the saturation occurs (~ 200 ms), the difference of the resolution appears but not becomes larger than $\sim 20\%$ in the total amplitudes (left).

as implemented in the study of Buonanno et al. (2005). “Upper bound” denotes the most optimistic estimation. In the case of $L_{\nu_e} = 6.5 \times 10^{52} \text{ erg s}^{-1}$, about 30 % of the available gravitational binding energy of the neutron star of $3 \times 10^{53} \text{ erg}$ may be emitted during the simulation of 500 ms followed here. From Figure 2 showing the monotonic increase of the neutrino-originated amplitudes, we multiply the amplitude for the case of “High rate” by an enhancement factor of 3 and consider it as an upper bound. Then from Figure 10, we may say that the background radiation considered here could be larger for the frequency above ~ 1 Hz than the upper limit of the background radiation generated in the inflationary epoch (the horizontal line in the figure). However, the frequency range is just outside the sensitivity of the proposed detectors, such as DECIGO (Seto et al. 2001).

4. Summary and Discussion

We presented the results of numerical experiments, in which we studied how the asphericities induced by the growth of the standing accretion shock instability could produce the gravitational waveforms in the postbounce phase of core-collapse supernovae. To obtain the neutrino-driven explosions, we parametrized the neutrino fluxes emitted from the central protoneutron star and approximated the neutrino transfer by the light-bulb scheme. By doing the spectrum analysis of the waveforms, we investigated the detectability of the signals from a single core-collapse supernova and the cosmological ones by the ground-based

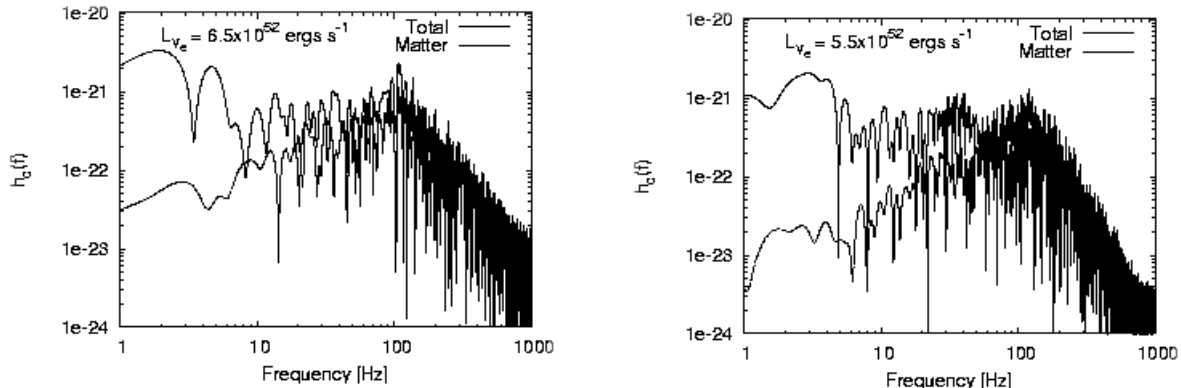


Fig. 8.— Spectral distributions of the gravitational waves from the sum of anisotropic neutrino emissions and matter motions (thick line), and only from the matter motions (dotted line) for the case of $L_{\nu_e} = 6.5$ (left) and 5.5×10^{52} erg s $^{-1}$ (right), respectively. It can be seen the dominance of the neutrino-originated gravitational waves at the lower frequency of ~ 100 Hz.

and space-based laser interferometers, respectively. Our main results can be summarized as follows.

1. The amplitudes of the gravitational waves from the anisotropic neutrino emissions are larger up to two orders of magnitudes than the ones from the matter motions during the SASI operations. It is found that the wave amplitudes from the neutrinos show the monotonic increase with time, regardless of the neutrino luminosities from the protoneutron star. We point out that this feature can be understood by the specific nature of SASI, which makes the deformation of the shock waves of $l = 1, 2$ modes dominant, leading to the enhanced neutrino emissions in the regions close to the symmetry axis. In fact, we show that the amplitudes become larger when the growth of the SASI enters the nonlinear phase, in which the deformation of the shocks and the neutrino anisotropy become large.

2. From the spectrum analysis of the waveforms, we find that the amplitudes from the anisotropic neutrino emissions are dominant over the ones from the matter motions at frequency $\lesssim 100$ Hz. The detection of such signals from a galactic supernova may be marginal for the currently running detector of the first LIGO and promising for the detectors in the next generation such as LCGT and the advanced LIGO.

3. As for the background radiation, we indicate that the contribution of the gravitational signals considered here could be larger at frequency $\gtrsim 1$ Hz than the primordial gravitational wave backgrounds generated in the inflationary epoch. Unfortunately, however, it is found that this frequency range is just outside of the sensitivity of the proposed detectors, such as

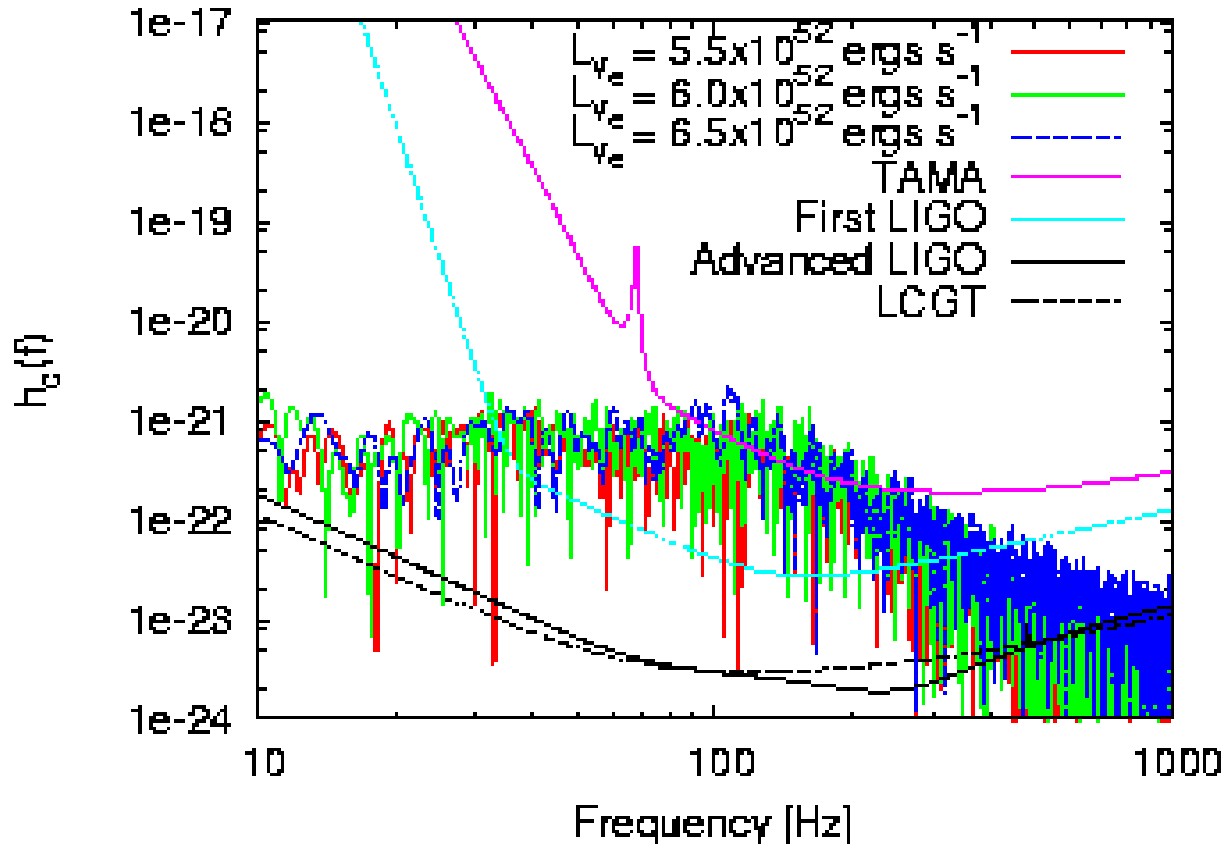


Fig. 9.— Detection limits of TAMA (Ando & the TAMA collaboration 2002), first LIGO (Thorne 1995), advanced LIGO (Weinstein 2002), and Large-scale Cryogenic Gravitational wave Telescope (LCGT) (LCGT Collaboration 1999) and the expected gravitational wave spectra. The source is assumed to be located at the distance of 10 kpc.

DECIGO.

We give a brief comparison with recently published models. The monotonic increase with time in the wave amplitudes of the neutrino-originated gravitational waves is consistent with the model s15r of Müller et al. (2004), in which the operation of the SASI was seen. However, the amplitudes here are typically larger (up to 1 order of magnitude). This should be mainly because the neutrino luminosity here is taken to be higher than the one obtained in Müller et al. (2004), which is about $\sim 2 \times 10^{52}$ erg/s during the SASI operation. As for the total gravitational-wave energy emission, typical values of the computed models here ($\sim 10^{-10} M_{\odot} c^2$, see Table 1) are one order magnitude smaller than the one in Müller et al. (2004). This should be owing to the excision of the protoneutron star, by which the contribution from the high frequency domain of the energy emissions are eliminated in

this study. It should be noted that the larger oscillations of the protoneutron star in the postbounce phase (Burrows et al. 2006) and the resulting efficient gravitational emissions (Ott et al. 2006) cannot be treated in principle here.

The simulation highlighted here is nothing but an idealized study for the physical understanding of relation between the asphericities induced by the SASI and the resulting gravitational waves. Remembering the caveats about the assumptions of the artificially constructed initial condition, the fixed accretion rate, the absorbing boundary condition, and the fixed neutrino luminosity and energies, it is by no means definitive at all. Especially, much better neutrino transfer is indispensable for more reliable calculations of the neutrino-originated gravitational wave, which we only considered the radial transport. One more major deficit is the axial symmetry assumed in the present two-dimensional (2D) simulations. In three-dimensional environments, the pronounced dominance of $l = 1, 2$ along the symmetry axis, which is a coordinate singularity in the 2D computations, may become weaker, owing to the additional spatial degree of freedom in the azimuthal (ϕ) direction. In the 3D case, we think that the qualitative features of the plus mode waveform computed in the 2D case here will be unchanged, but quantitatively, we expect that the amplitudes become smaller owing to the reduced anisotropy along the symmetry axis. Thus the amplitudes calculated in this study could be an upper bound, in which the maximal anisotropy of the shock waves and thus neutrino emissions outside the neutrino sphere could be achieved. Furthermore we think that it is interesting to investigate the properties of the cross mode gravitational waves, which are of genuine 3D origin and could be possibly produced from the transfer of the $l = 1, 2$ modes to some modes with nonvanishing m in Y_{lm} . This study is a prelude to the forthcoming 3D simulations to clarify those aspects, which will be presented elsewhere.

K.K. expresses thanks to T. Takiwaki, Y. Suwa for useful discussions, T. Hiramatsu for informative discussions with respect to the gravitational-wave backgrounds, and K. Sato for continuing encouragements. The numerical calculations were partially done on the supercomputers in RIKEN and KEK (KEK supercomputer Projects No.02-87 and No.03-92). This work was supported in part by Grants-in-Aid for the Scientific Research from the Ministry of Education, Science and Culture of Japan (No.S14102004, No.14079202, No.14740166), and Grant-in-Aid for the 21st century COE program “Holistic Research and Education Center for Physics of Self-organizing Systems”.

REFERENCES

- Ando, M., & the TAMA collaboration 2002, *Classical and Quantum Gravity*, 19, 1409
- Ando, M., et al. 2005, *Classical and Quantum Gravity*, 22, 1283
- Ando, S., & Sato, K. 2004, *New Journal of Physics*, 6, 170
- Abbott, B., et al. 2005, *Phys. Rev. D*, 72, 122004
- Bazan, G. & Arnett, D. 1998, *ApJ*, 496, 316
- Blondin, J. M., Mezzacappa, A., & DeMarino, C. 2003, *ApJ*, 584, 971
- Blondin, J. M., & Mezzacappa, A. 2006, *ApJ*, 642, 401
- Braginskii, V. B., & Thorne, K. S. 1987, *Nature*, 327, 123
- Buras, R., Rampp, M., Janka, H.-T., & Kifonidis, K. 2003, *Physical Review Letters*, 90, 241101
- Burrows, A. & Hayes, J. 1996, *Physical Review Letters*, 76, 352
- Burrows, A., Young, T., Pinto, P., Eastman, R., & Thompson, T. A. 2000, *ApJ*, 539, 865
- Burrows, A., Livne, E., Dessart, L., Ott, C. D., & Murphy, J. 2006, *ApJ*, 640, 878
- Buonanno, A., Sigl, G., Raffelt, G. G., Janka, H.-T., Müller, E. 2005, *Phys. Rev. D*, 72, 084001
- Buonanno, A, Boulder 2002, *Particle physics and cosmology*, 855-892. gr-qc/0303085
- Dimmelmeier, H., Font, J. A., Müller, E. 2002, *A&A*, 393, 523
- Epstein, R. 1978, *ApJ*, 223, 1037
- Fryer, C. L., Holz, D. E., & Hughes, S. A. 2002, *ApJ*, 565, 430
- Fryer, C. L. 2004, *ApJ*, 601, L175
- Fryer, C. L., Holz, D. E., & Hughes, S. A. 2004, *ApJ*, 609, 288
- Flanagan, É. É., & Hughes, S. A. 1998, *Phys. Rev. D*, 57, 4566
- Hannestad, S., & Raffelt, G. 1998, *ApJ*, 507, 339
- Haxton, W. C. 1988, *Physical Review Letters*, 60, 1999

- Heger, A., Woosley, S. E., & Spruit, H. C. 2005, *ApJ*, 626, 350
- Hiramatsu, T., Kotake, K., Kudoh, H., & Taruya, A. 2005, *MNRAS*, 364, 1063
- Janka, H.-T., & Mueller, E. 1996, *A&A*, 306, 167
- Kifonidis, K., Plewa, T., Scheck, L., Janka, H.-T., Müller, E. 2006, *A&A*, 453, 661
- Kotake, K., Yamada, S., & Sato, K. 2003, *ApJ*, 595, 304
- Kotake, K., Yamada, S., & Sato, K. 2003, *Phys. Rev. D*, 68, 044023
- Kotake, K., Yamada, S., Sato, K., Sumiyoshi, K., Ono, H., & Suzuki, H. 2004, *Phys. Rev. D*, 69, 124004
- Kotake, K., Sato, K., & Takahashi, K. 2006, *Reports of Progress in Physics*, 69, 971
- LCGT Collaboration, *Int. J. Mod. Phys. D*, **5**, 557, (1999).
- Liebendörfer, M., Mezzacappa, A., Thielemann, F.-K., Messer, O. E., Hix, W. R., & Bruenn, S. W. 2001, *Phys. Rev. D*, 63, 103004
- Malek, M., et al. 2003, *Physical Review Letters*, 90, 061101
- Mönchmeyer, R., Schaefer, G., Mueller, E., & Kates, R. E. 1991, *A&A*, 246, 417
- Meakin, C. A., & Arnett, D. 2006, *ApJ*, 637, L53
- Müller, E., Rampp, M., Buras, R., Janka, H.-T., & Shoemaker, D. H. 2004, *ApJ*, 603, 221
- Mueller, E., & Janka, H.-T. 1997, *A&A*, 317, 140
- New, K. C. B. 2003, *Living Reviews in Relativity*, 6, 2
- Obergaulinger, M., Aloy, M. A., Müller, E. 2006, *A&A*, 450, 1107
- Ott, C. D., Burrows, A., Livne, E., & Walder, R. 2004, *ApJ*, 600, 834
- Ott, C. D., Burrows, A., Thompson, T. A., Livne, E., & Walder, R. 2006, *ApJS*, 164, 130
- Ott, C. D., Burrows, A., Dessart, L., & Livne, E. 2006, *Physical Review Letters*, 96, 201102
- Ohnishi, N., Kotake, K., & Yamada, S. 2006, *ApJ*, 641, 1018
- Ohnishi, N., Kotake, K., & Yamada, S. 2006, submitted to *ApJ*
- Phinney, E.S, 2001, preprint astro-ph/0108028

- Ruffert, M., Janka, H.-T., & Schaefer, G. 1996, *A&A*, 311, 532
- Scheck, L., Plewa, T., Janka, H.-T., Kifonidis, K., Müller, E. 2004, *Physical Review Letters*, 92, 011103
- Schinder, P. J., Schramm, D. N., Wiita, P. J., Margolis, S. H., & Tubbs, D. L. 1987, *ApJ*, 313, 531
- Segalis, E. B., & Ori, A. 2001, *Phys. Rev. D*, 64, 064018
- Seto, N., Kawamura, S., & Nakamura, T. 2001, *Physical Review Letters*, 87, 221103
- Shibata, M., & Sekiguchi, Y. 2004, *Phys. Rev. D*, 69, 084024
- Shen, H., Toki, H., Oyamatsu, K., Sumiyoshi, K. 1998, *Nuclear Physics*, A637, 43, 109, 301
- Stone, J. M. & Norman, M. L. 1992, *ApJS*, 80, 753
- Thorne, K.S., Gravitational Waves. In *Proceedings of the Snowmass 95 Summer Study on Particle and Nuclear Astrophysics and Cosmology*, World Scientific, pp. 398-425, (1995).
- Turner, M. S. 1978, *Nature*, 274, 565
- Turner, M. S. 1997, *Phys. Rev. D*, 55, 435
- Weinstein, A. 2002, *Classical and Quantum Gravity*, 19, 1575
- Yamada, S., & Sato, K. 1995, *ApJ*, 450, 245
- Yamasaki, T., & Yamada, S. 2005, *ApJ*, 623, 1000
- Yamasaki, T., & Yamada, S. 2006, accepted to *ApJ*
- Zwerg, T., & Mueller, E. 1997, *A&A*, 320, 209

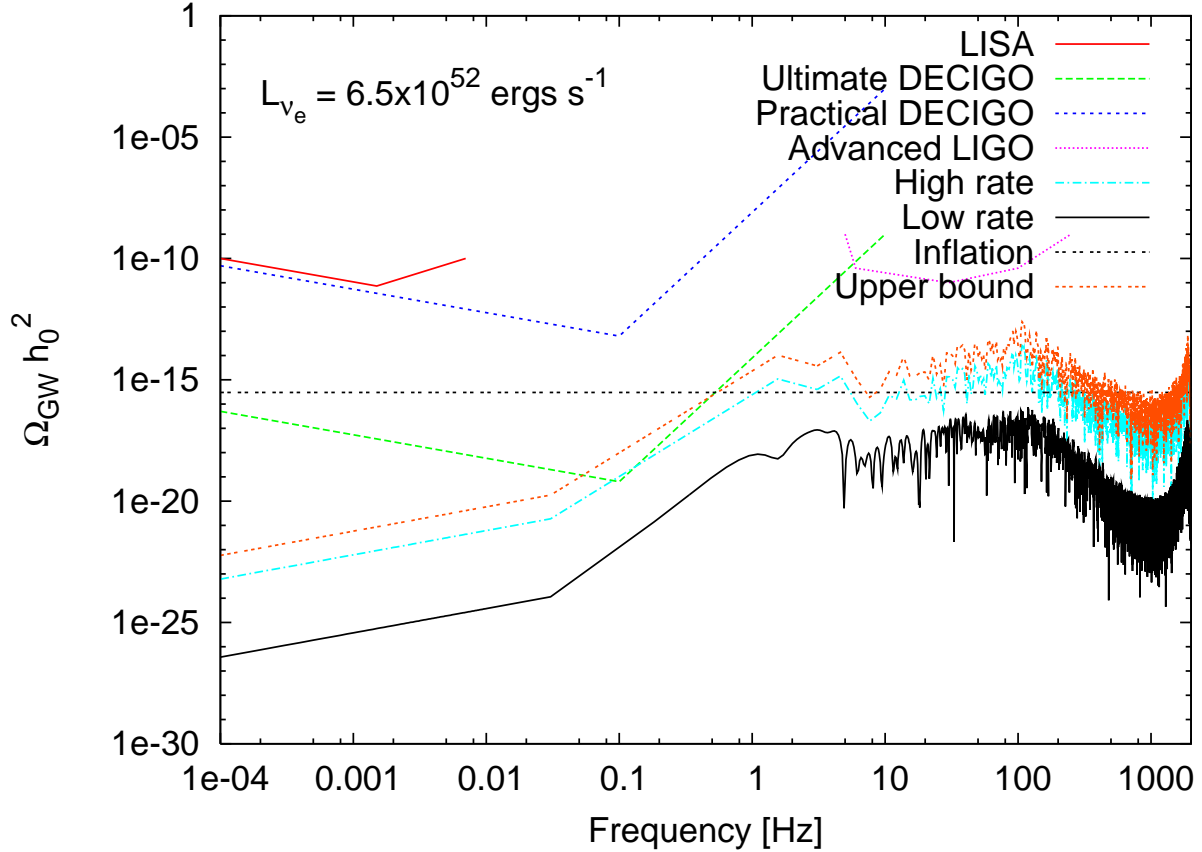


Fig. 10.— Cosmological gravitational wave background for the highest luminosity case of $L_{\nu_e} = 6.5 \times 10^{52} \text{ erg s}^{-1}$, taking into account the possible enhancement due to the uncertainty of the cosmic star formation rate labeled by “Low rate” and “High rate”, and the limited simulation time labeled by “Upper bound” (see text for details), with some indicated sensitivity curves for future missions of LISA, the LIGO in the third generation (Buonanno et al. 2002), and practical/ultimate DECIGO (Seto et al. 2001). The horizontal line indicates a maximum version of gravitational wave backgrounds produced during the slow-roll inflation assuming $T/S = 0.3$ for the ratio of tensorial and scalar contributions to the cosmic microwave background radiation anisotropy (Turner 1997), concreted in Buonanno et al. (2005).